ADVANCED INTELLIGENT SYSTEMS
Open Access
www.advintellsyst.com

Self-Sensing Robotic Structures from Architectured Particle Assemblies

*Xudong Yang, Zongzheng Wang, Bojian Zhang, Tianyu Chen, Changhong Linghu, Kunlin Wu, Guohui Wang, Hailu Wang, and Yifan Wang**

The tight coupling of shape transformation, stiffness tuning, and self-sensing that biological organisms exhibit has long served as inspiration for next-generation soft robots. However, most current soft robots rely on intrinsically soft materials for actuation, separately embedded sensors for sensing, and have fixed stiffness once fabricated. Large gaps remain between these soft robots and biological organisms where multifunctionality is realized within an integrated body. Herein, a new class of robotic structures from architectured particle assemblies is introduced. They combine three functions: shape changing, stiffness variation, and self-sensing into one monolithic structure. Unlike traditional entirely soft robots, the design utilizes the geometric contacts of stiff, architectured particles under confining pressure to achieve these functions. The applications of these structures by designing smart self-sensing architectures and soft grippers are demonstrated. The design provides a new paradigm of multifunctional robotic structures, with potential multiscale applications in adaptive robots, smart devices, and reconfigurable architectures.

1. Introduction

Achieving biomimetic materials and structures that can reversibly switch their geometries, actively or passively vary stiffness, and sense external stimuli has long been a target for designing next-generation soft robots.[1] Robotic materials and structures with these functions have been predominant to realize distinguished applications, ranging from soft actuators,[2] and wearable electronics,[3] to reconfigurable robots.[4] However, one of the main distinctions between living organisms and existing artificial robots is that the former can achieve multifunctionality with their integrated body structures,[5] while the latter requires separately assembled components including actuators, sensors, and control systems to function. Integrating shape morphing, stiffness variation, and self-sensing abilities into an adaptive monolithic structure is highly desirable, as it eliminates the potential mechanical mismatch and delamination of separately bonded actuator/sensor components,[5] while significantly improving manufacturing scalability. Nevertheless, material and structure designs that can accommodate these multiple functions within unified bodies remain limited.[5]

In soft robots that can achieve reversible shape morphing, the elasticity (e.g., bendability[6]) and elastic instability (e.g., buckling[7] and snapping[8] instabilities) of materials have been utilized. However, these require the softness of either the intrinsic material (i.e., low Young's modulus) or the resulting structure (e.g., thin shells or slender beams).[9] The inborn softness limits their applications where tunable stiffness is required.[10] For example, bioinspired soft robots (e.g., elephant trunks and octopus tentacles inspired) need to be soft and compliant for safe interactions with environments and to be stiffened when manipulating heavy objects.[11] One approach to solving the intrinsic trade-off between high morphing ability and low stiffness tunability is to modulate the mechanical properties with responsive materials driven by stimuli such as temperature,[12] magnetic field,[13] or electric field.[14] Nevertheless, these methods either require large temperature changes to activate a slow-phase transition (e.g., shape memory polymers[15]) or involve high magnetic/electrical fields that are not easily achievable (e.g., magnetorheological materials[16] and electroactive polymers[17]). Another approach is to utilize jamming transition of discrete granular particles, laminar, or fiber structures between fluid-like plasticity and solid-like rigidity.[18] However, it is challenging to achieve programmed and reversible shape morphing by jamming because of the highly disordered characteristics of their underlying structures.[19]

Besides shape morphing and stiffness tuning, robotic materials and structures are expected to perceive their own shape and sense external stimuli.[5d,20] Current structural sensing technologies largely rely on adopting layered structures (Table S1, Supporting Information), in which the morphing/stiffening layer and the sensing layer are bonded together.[21] However, the mechanical mismatch between the sensing and the actuation layer usually leads to delamination.[22] Other methods involve using smart sensing

X. Yang, Z. Wang, B. Zhang, T. Chen, C. Linghu, K. Wu, G. Wang, H. Wang, Y. Wang
School of Mechanical and Aerospace Engineering
Nanyang Technological University
Singapore 639798, Singapore
E-mail: yifan.wang@ntu.edu.sg

The ORCID identification number(s) for the author(s) of this article can be found under https://doi.org/10.1002/aisy.202200250.

© 2022 The Authors. Advanced Intelligent Systems published by Wiley-VCH GmbH. This is an open access article under the terms of the Creative Commons Attribution License, which permits use, distribution and reproduction in any medium, provided the original work is properly cited.

DOI: 10.1002/aisy.202200250

materials like liquid–metal elastomers for both actuation and self-sensing without introducing extra components.[20b,23] However, liquid metals cannot work at temperatures below the melting point. Thus, it would be highly desirable to develop multifunctional robotic materials and structures that integrate morphing, stiffness tuning, and sensing within one integrated body.

To address this problem, nature has been a source of inspiration as biological creatures including scorpions, spiders, and vertebrates have rigid structured skeletons or shells connected with soft materials (i.e., muscles and skins) for integrated shape transformation and sensing.[24] The rigidly structured frameworks are made of solid, discrete building blocks[24b–d,25] which can be found widely in nature, from the microscale layers in nacre,[24b] the millimeter-scale armadillo armors,[24c] to the macroscale plates in turtle shells[24d] (**Figure 1**a). These rigid building blocks can rotate, slide, assemble, and separate within a soft matrix, providing a feasible way to reconfigure the morphology and tune properties at the macroscale.[24b–d,25]

Inspired by this fascinating design of biological structures made of rigid building blocks connected with soft materials, in this article, we present morphable, stiffness-tunable, and self-sensing robotic structures from architectured particle assemblies. Unlike continuous soft material systems, macroscale deformation is achieved by the relative motions and dislocations of discrete architectured particles bonded by soft membranes in our system.[26] With these discrete architectured particles, more internal degrees of freedom of the structures are released.[27] By designing the geometry of individual particles, we demonstrate the reversible shape-morphing ability of our structures with zero, positive, and negative Gaussian curvatures under the activation of confining pressure. Our structure can transform from a soft state to a rigid state under boundary confinement. Furthermore, instead of coupling to extrastrain sensors, we coat the particle surfaces with conductive layers and demonstrate the structures' self-sensing ability. Our design seamlessly integrates shape morphing, stiffness tuning, and piezoresistive sensing into one monolithic structure of "three-in-one" functionality and offers a platform for reconfigurable architectures, soft robotics, smart wearables, etc.

2. Results and Discussions

2.1. Design Principles and Fabrication Procedures

To decompose a curved surface into discrete particles, we utilize a tessellation method and choose trapezoidal particles as our

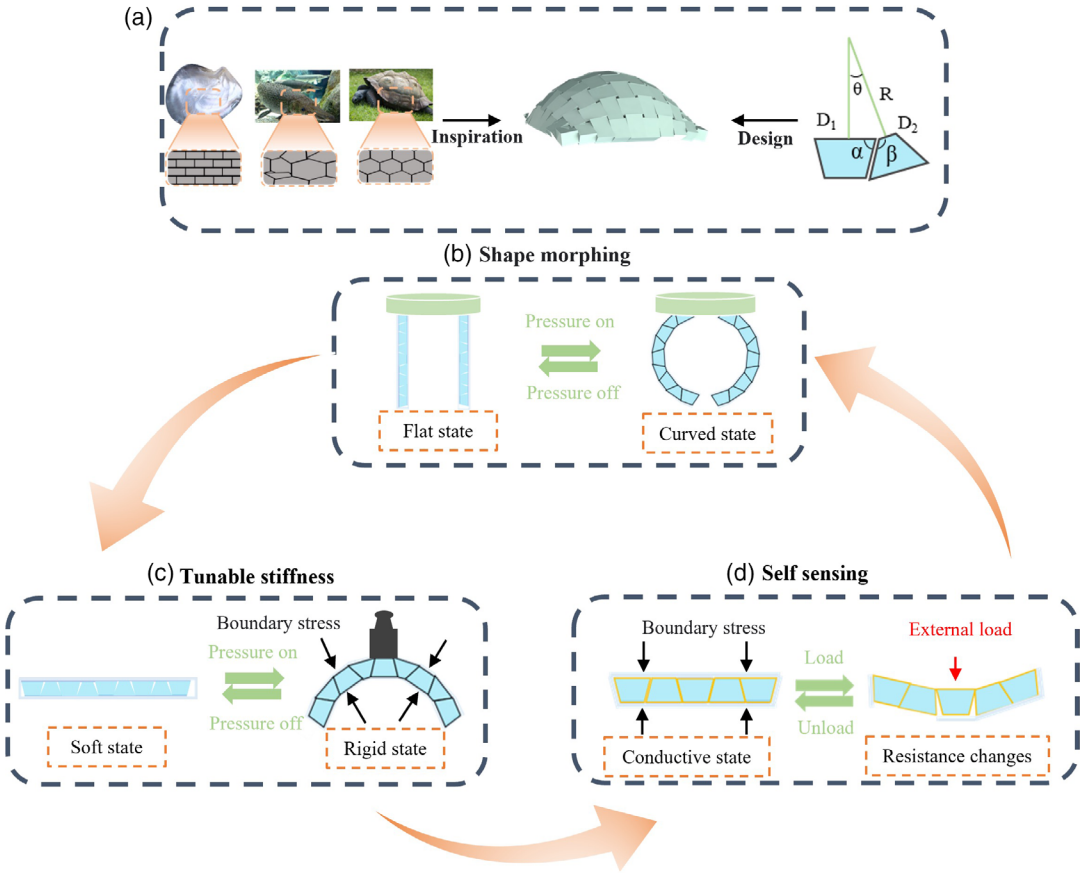


Figure 1. Schematic illustrations of morphable, stiffness-tunable, and self-sensing robotic structures from architectured particle assemblies. a) Morphable, stiffness-tunable, and self-sensing structures inspired by nature which can be designed from architectured particles. b) Programmed discrete architectured particles enclosed in the rubber envelope with shape-morphing ability activated by negative pressure (gripper shape). c) Varying the stiffness by negative pressure. d) Self-sensing ability via surface-conductive architectured particles.

© 2022 The Authors. Advanced Intelligent Systems published by Wiley-VCH GmbH

basic elements (Figure 1a, see Experimental Section). Trapezoidal particles possess large contact surfaces[24b] and are widely used in architectured materials for enhanced mechanical performance.[28] Following the geometrical construction principles,[29] a center angle θ can be obtained when the two trapezoidal particles with different tilting angles (α and β) are in contact (Figure 1a).

$$\theta = \alpha + \beta - \pi \tag{1}$$

With n pairs of particles, a curved surface can be obtained (See Experimental Section). The designed particles are 3D printed with stereolithography (SLA) method. Printed particles are enclosed in an air-tight rubber envelope (thickness: 0.2 mm) in designed order and then connected to a vacuum pump with a soft tube. The discrete particle assemblies are weakly coupled by the envelope which can easily be bent and twisted (Figure S1, Supporting Information). To trigger the reversible shape transformation, we apply negative pressure to the rubber envelope. With increasing negative pressure, the discrete particles form surface contacts with their neighbors, transforming from the initial flat state to the targeted curved shape. When negative pressure is removed, the curved structure will return to the flat, relaxed shape under gravity and the elasticity of the envelope (Figure 1b). Additional fabrication information can be found in Experimental Section, and Figure S2, Supporting Information, provides a fabrication process illustration.

Besides shape changing, the confining pressure at boundaries also increases the apparent bending modulus of the assembled structure due to enhanced contact between neighboring particles (Figure 1c). Compared with most continuous shape-morphing materials triggered by heat or other stimuli with slow actuation speed,[9a] our robotic structures could achieve shape morphing and stiffen simultaneously with a fast response time (≈0.3 s for actuation and ≈0.4 s for recovery, Movie S1, Supporting Information). Moreover, the enhanced contacts between particles under confining boundary stress provide a way to sense through their contact resistance in our robotic structures. To achieve this, we manufacture surface conductive particles by sputter coating a uniform thin conductive Au layer (≈22 nm thick, see Experimental Section) on the surface. Under the confining boundary stress, the assembled conductive particles form a conductive path. Once a load is applied, the contact resistance between particles will change, leading to a change in the overall resistance (Figure 1d). Unlike traditional layered structures that integrate sensing layers and actuation layers with easily delaminated interfaces (Table S1, Supporting Information), our robotic structures achieve shape morphing, stiffening, and self-sensing within one integrated body.

2.2. Shape Morphing and Stiffness Tunability

In our design, rapid shape morphing (≈0.3 s for actuation and ≈0.4 s for recovery, Movie S1, Supporting Information) can be achieved by quickly applying negative pressure to the structure. As a demonstration of the concept, we start by producing 1D arc-shaped structures (**Figure 2**a). We tessellate the arc surface into trapezoidal particles and arrange the architectured particles into the rubber envelope. When the boundary confining pressure is applied, the discrete particles move in contact with each other and assemble into the arc shape. We also create a hook shape with varying curvature along the length direction to show the versatility of our design (Figure 2a). Not limited to curved surfaces with zero Gaussian curvatures, we expand our design to 2D surfaces with non-zero Gaussian curvatures. We first tessellate positive and negative Gaussian curvature surfaces into particle assemblies using a method described in a recent work.[30] The 3D-printed particles from the tessellation can then be deployed to the designed curved surfaces with negative pressure. Unlike continuous materials where geometric frustration may occur when deformed into non-zero Gaussian curvatures, in our design, the particles can move easily because of their discrete nature and the structure can be deployed quickly upon activation (Figure 2a). When negative air pressure is applied, the soft rubber film will wrinkle and shrink along with the movement of the particles. The rubber film will locally deform under pressure. Figure S3, Supporting Information, shows the deformation of the rubber membrane under negative pressure in the saddle surface. As the wrinkled membranes have smaller tensile stiffness compared with the flat state, it means that membrane contribution to the overall apparent bending stiffness is even less than what is estimated in Experimental Section.

To quantify the stiffness tunability of our structures as a function of increasing boundary confining pressure, we design structures that will remain flat under pressure and perform three-point bending tests to measure their apparent bending modulus. The height of the particles is set to 7.5 mm for all the samples, and the length of the square medial section is set to 10 mm for all the samples. (Figure S4, Supporting Information, see Experimental Section). We first analyze the mechanical response of particle assemblies with tilting angles $\alpha = 60°$–$80°$ under 0 and 80 kPa with three-point bending experiments and finite element analysis (FEA) method (Figure 2b,c). The FEA results and the experimental results are in good agreement with error. The deviation may be due to the estimation mismatch in the material properties and the frictional coefficients. Moreover, it is found that our structures exhibit elastoplastic behaviors under negative pressure. Unlike fiber or layer jamming,[31] no distinct slip point is observed throughout the loading process in our structure. However, microscale rotations and rearrangements of particles may occur, resulting in the yielding of the structure and hysteresis loop during the loading–unloading cycle[18a,31] (Figure S5, Supporting Information). To quantify the influence of particles' geometric parameters on the mechanical response, we analyze the slope of the initial linear regimes at small indentation displacements (0.2 mm) governed by the elastic behavior under different confining pressures and tilting angles. The apparent elastic bending modulus E_b can be calculated as[18a]

$$E_b = \frac{Kl^3}{4bh^3} \tag{2}$$

where K is the slope of the initial elastic regime from the force–displacement curve of the three-point bending test, and l, b, h are the length between the support span, width, and height of the sample, respectively. For particles with a tilting angle of $\alpha = 60°$, the apparent bending moduli increase from ≈1.7 to

© 2022 The Authors. Advanced Intelligent Systems published by Wiley-VCH GmbH

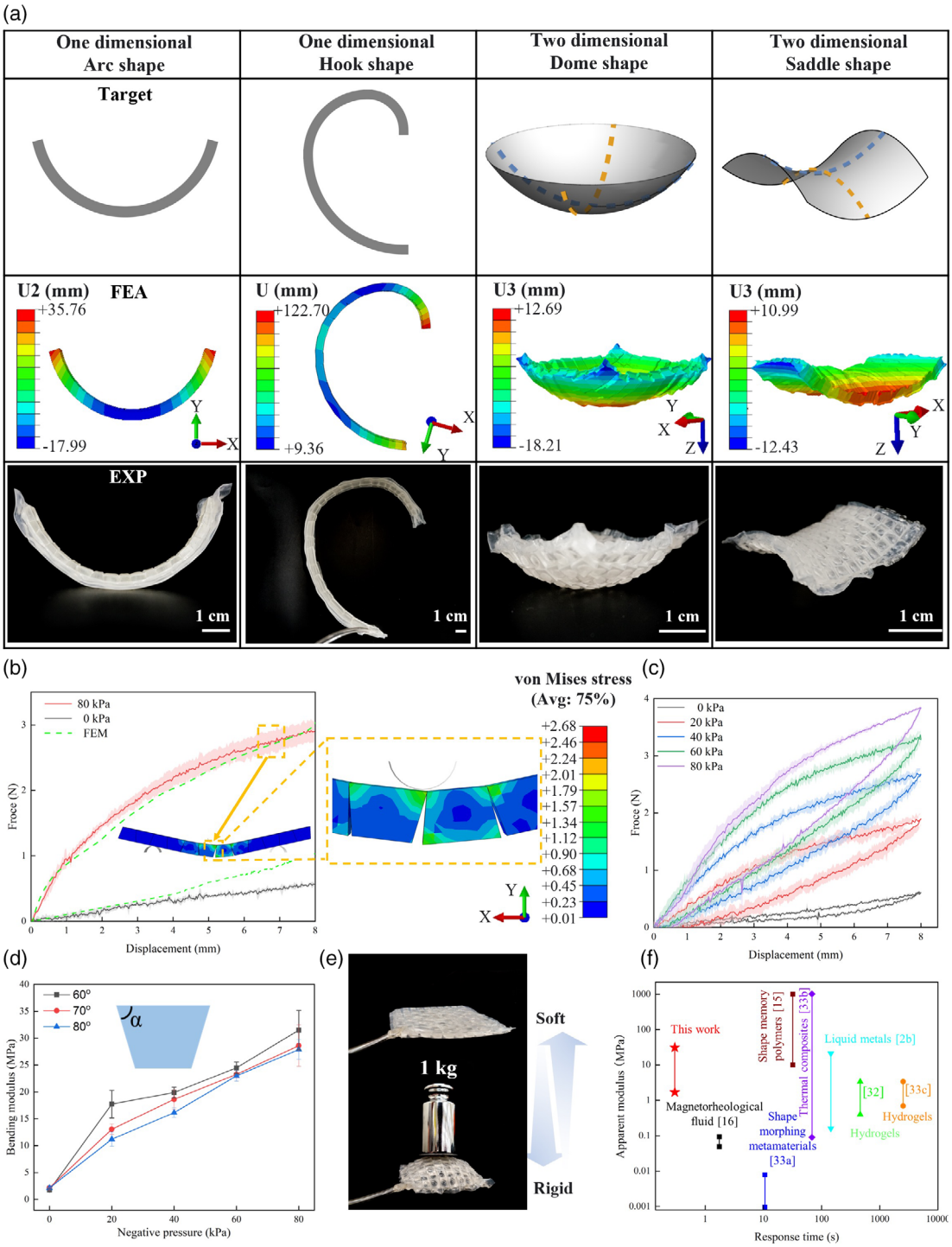


Figure 2. Actuation and mechanical properties of robotic materials. a) FEA and experimental results for zero Gaussian curvature arc shape and hook shape; positive Gaussian curvature dome shape; and negative Gaussian curvature saddle shape. Color bars represent the displacements along U2 (*y*-axis) and U3 (*z*-axis) directions. b) Comparison of FEA and experimental results under three-point bending tests. The inset shows the FEA plots indicating the deformation and stress contour of the robotic structure under three-point bending test; color bars represent von Mises stress within the structure from FEA. c) Force–displacement curves of the structure under various confining pressures via three-point bending test. The colored line represents the average values and the shaded areas represent the standard deviation between the three different tests. d) Effects of tilting angle on the apparent bending moduli under various confining pressure. The error bars are standard deviations obtained from three separate experiments. e) Demonstration of the soft-to-stiff transformation under confining pressure (weight: 1 kg, confining pressure: 80 kPa). f) Tunable apparent modulus versus response time for materials with shape programmability and tunable stiffness. The solid lines represent the range of tunability in each reference. Photo credit: Bojian Zhang and Xudong Yang, Nanyang Technological University.

© 2022 The Authors. Advanced Intelligent Systems published by Wiley-VCH GmbH

≈31 MPa by over 18 times, with the confining pressure increasing from 0 kPa to 80 kPa. Unlike jamming structures where there is a distinct transition,[18a] the stiffness increases almost linearly with the confining pressure in our case (Figure 2d). Moreover, the apparent bending modulus decreases with increasing tilting angle α. This is because larger tilting angles make the structure open smaller gaps under loading, which costs less energy and results in a lower apparent bending modulus. To demonstrate the stiffness tunability, we place a 1 kg weight on our structure. When negative pressure (80 kPa) is applied, it becomes stiff enough to support the weight without significant[32] deformation (Figure 2e). Compared with other materials with active shape programmability and tunable stiffness, such as shape memory polymers, liquid metals, magnetorheological materials, or hydrogels,[2b,15,16,32,33] (Figure 2f and Table S2, Supporting Information), our robotic structures have the advantage of fast response (≈0.3 s for actuation and ≈0.4 s for recovery, Movie S1 and S2, Supporting Information) without the need of thermal or magnetic actuation sources which are undesirable in many practical applications.

2.3. Self-Sensing Ability

Robotic structures are expected to perceive their own shape and sense external stimuli for automatic and intelligent interaction with surroundings.[1,34] In our design, we use sputter coating to generate a thin conductive gold layer (≈22 nm) on the architectured particles (**Figure 3**a, see Experimental Section).[35] The bonding strength between the metal layer and the polymer layer varies with the sputter-coating parameters (e.g., sputtering time) and the polymer surface properties.[36] For the gold sputter coating on the polymer, the adhesion strength ranges from 6.4 MPa to more than 35 MPa,[36,37] which is larger than the stress in the three-point bending simulation. The morphology of the surface and the resistivity of the conductive particles can be found in Figure S7 and S8, Supporting Information. With the surface-conductive particles, our structure can achieve self-sensing ability. First, in a relaxed state, the conductive particles are in loose contact with each other. The contact resistance between neighboring particles is too high to be measured by our instrument (>1 G Ohm), and the structure is insulated. When the confining pressure brings the particles into close contact, the contact resistance between two neighboring particles reduces to R_1 and the structure becomes conductive. Once loading is applied, the structure deforms and the particles rotate against their neighbors, resulting in concentrated contact forces at the particle edges. This high concentration of the contact force at edges further decreases the contact resistance between particles to r_1 (Figure 3b). The change in the contact resistance between particles at varying loads offers a feasible way to sense the structures' own deformation under external load.

To elucidate the working principle of our self-sensing structure, we utilize numerical methods[38] to investigate the contact between the surfaces of neighboring particles. With the obtained real contact area by elastic contact theory with conjugate gradient techniques,[38] the contact resistance between two conductive particles is calculated by the tunneling theory[39] (Figure S10, Supporting Information for details). We use two cubic particles to validate our model (Figure 3c). The contact resistance of the two cubic particles decreases with increasing pressure and the results of our model agree well with the experiment. After validation, we numerically investigate the real microscopic contact area changes of the trapezoidal particles under three-point bending. The contact forces between two particles are obtained from FEA and the forces are used to calculate the real contact area under three-point bending using the proposed method (Figure 3d). With the increase in loading displacements, the contact forces increase, and the real contact area also increases, which result in lower contact resistance.

We also investigate the structure's sensing performance with piezoresistive tests. We measure the resistance change of our structure with different numbers of conductive particles in three-point bending tests (Figure 3e). To characterize the sensitivity of our structure, the Gauge factor (GF) is employed and defined as

$$GF = \frac{\Delta R/R_0}{\varepsilon} \tag{3}$$

where $\varepsilon = \frac{6Dd}{l^2}$ is the flexural strain and l, D, and d are the support span, deflection of the indenter, and the height of the specimen, respectively. ΔR and R_0 are the change in resistance and the initial resistance, respectively.

Typically, the resistance will increase under deformation in flexible sensors.[40] However, it is observed that in our structure, the resistance exhibits a nonlinear, negative response as a function of strain. For the structure with three conductive particles, it exhibits the highest sensitivity ($GF = -5.28$) at a small strain range (0–0.5%), while the sensitivity decreases with increasing strain. With increasing deformation of our structure, the sensitivity further decreases ($GF = -1.78$ at $\varepsilon > 2\%$) as the contact region between particles reaches to a limit (Figure 3d). To investigate the influence of the numbers of conductive particles, we compared the sensitivity of our structure with 3, 5, and 7 conductive particles (Figure 3e). It is observed that with increasing numbers of conductive particles, the sensitivity also increases within the same strain range. This is because more conductive particles result in larger changes in the contact area under deformation. To test the recoverability and repeatability of our structure, we perform cyclic tests at different maximum flexural strains (1.4%, 2.8%, and 5.6%) (Figure 3f). The results show a good recoverability of our structure. The long-term stability of our structure is measured with ≈200 cycles (Figure S11, Supporting Information), in which excellent durability and repeatability are observed.

2.4. Applications

So far, we have created robotic structures that can change shape, vary stiffness, and self-sense from architectured particle assemblies. The multifunctionality of our robotic structures offers versatile applications in smart architectures and soft robotics.

With the capability to change shape, vary stiffness, and self-sense, we first demonstrate its potential application as smart architectures (**Figure 4**a,b). The ancient discipline of architectures for human accommodations has been extended significantly to smart architectures with structural responsiveness,

© 2022 The Authors. Advanced Intelligent Systems published by Wiley-VCH GmbH

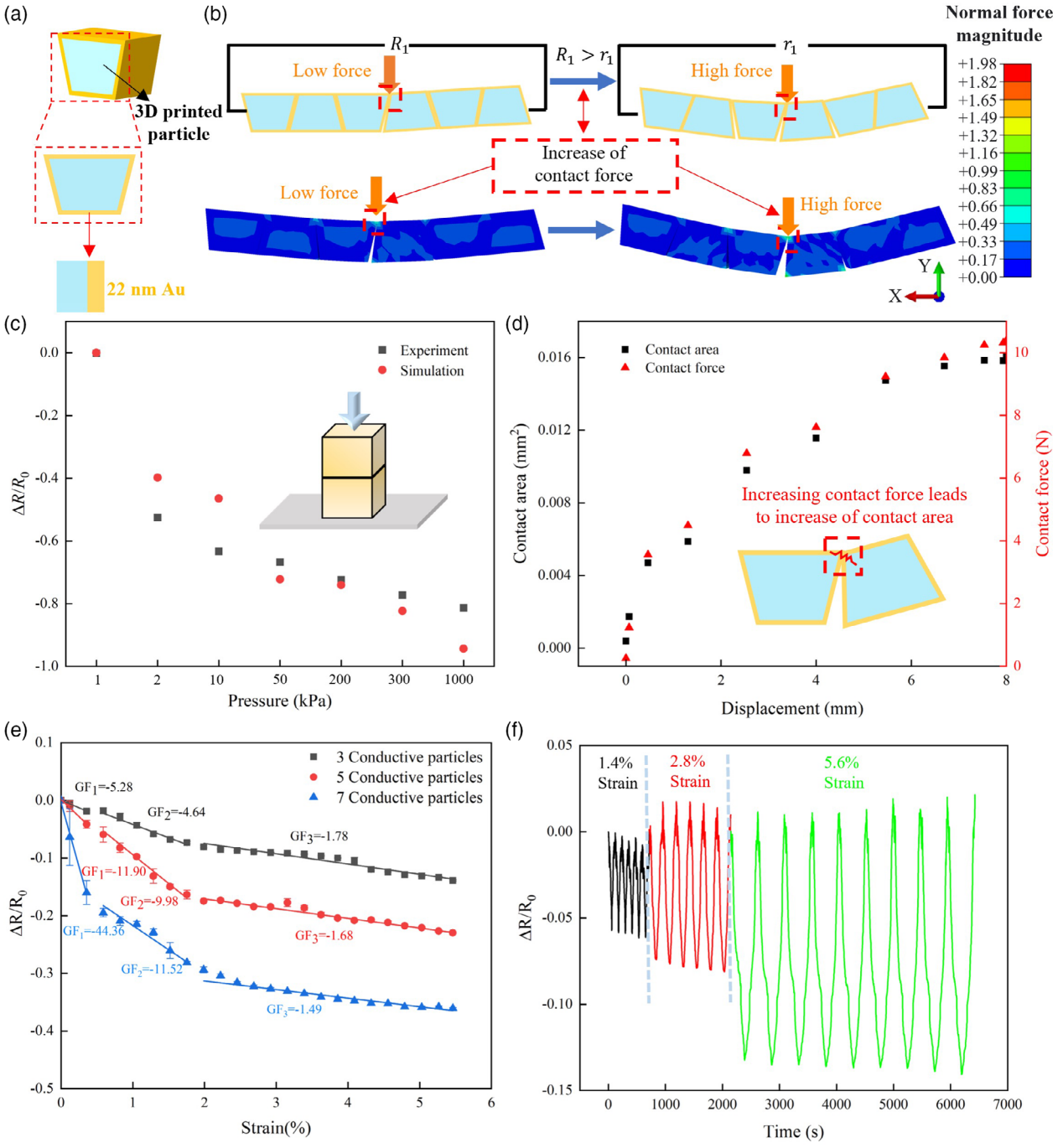


Figure 3. Self-sensing ability of the robotic structures. a) Cross section of the conductive particles. A thin gold layer (22 nm) is generated by sputter coating on the architecture particles. b) Schematic illustration of the sensing mechanism and FEA plots indicating the deformation and normal force contour under three-point bending test; color bar represents the magnitude of normal force within the neighboring particles. c) Simulation and experimental results of the resistance change for two cubic particles under loading. d) The increase of the contact force in FEA and the increase of the contact area in simulation for two trapezoidal particles under three-point bending. e) Sensitivity of the samples with different numbers of conductive particles. f) Resistance change under cyclic tests of different strains (three conductive particles, six cycles for 1.4% and 2.8% strain, and ten cycles for 5.6% strain).

adaptivity, and intelligent detection.[41] Existing solutions for smart architectures with sensing abilities require installing and distributing large numbers of external sensors or strain gauges for strain, deformation, and crack detection.[42] In our work, the robotic structures can not only be deployed from a flat shape to predesigned architectures (Figure 4a) but also detect the applied load without the need for external strain sensors. Figure 4a shows the loading capacity of our robotic structures

© 2022 The Authors. Advanced Intelligent Systems published by Wiley-VCH GmbH

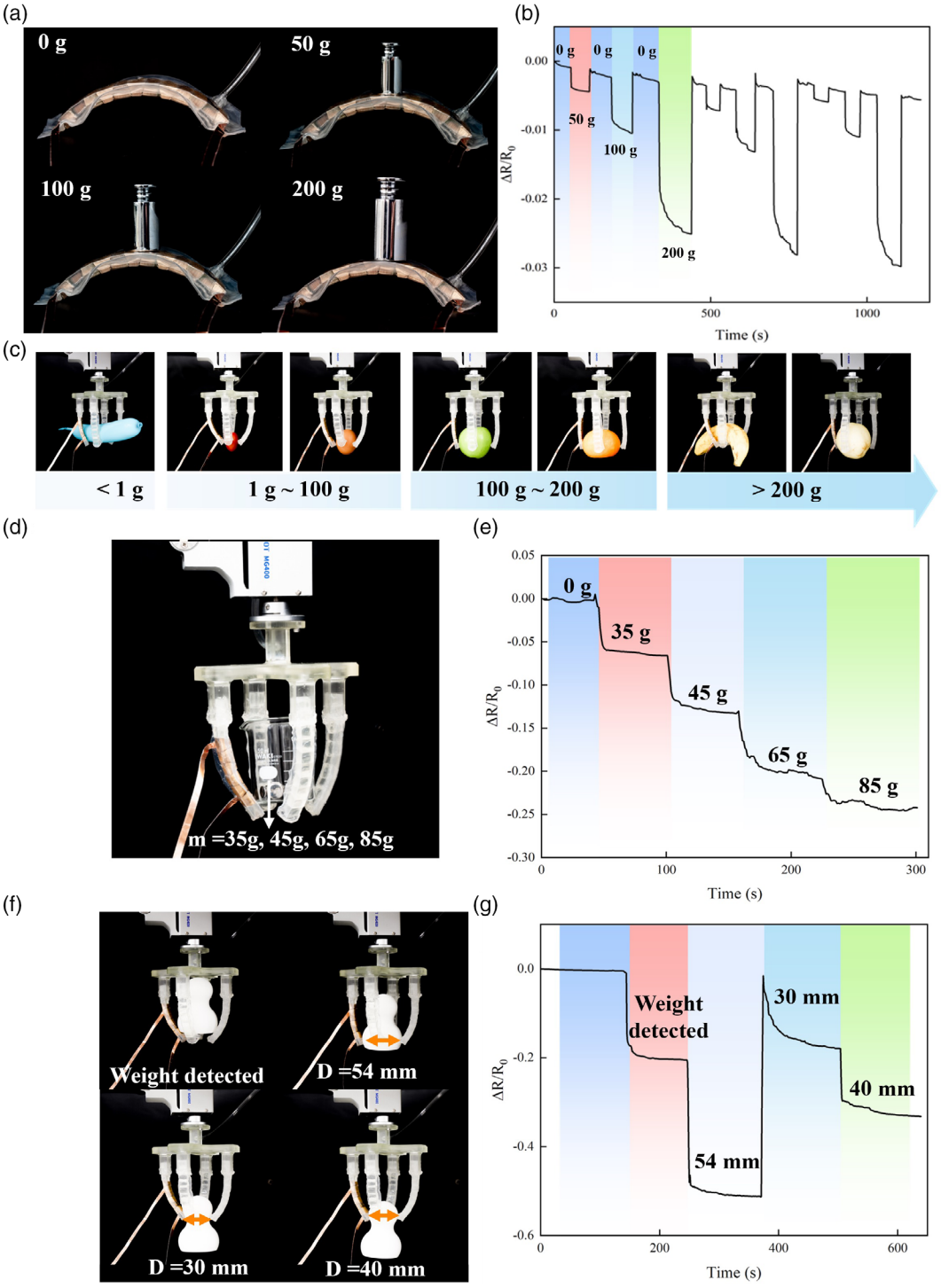


Figure 4. Applications of the robotic structures. a) Demonstration of smart architecture applications of our robotic materials. The smart arc-shape architecture under 0, 50, 100, and 200 g loadings. b) The corresponding resistance changes under different loadings. c) Demonstration of load capacity and good shape adaptivity by a soft gripper made with our robotic structures, grasping of objects (From left to right: a balloon, a tomato, an egg, an apple, an orange, a banana, and a pear) with arbitrary shapes, and various weights ranging from less than 1 g to more than 200 g. d) Demonstration of weight-sensing ability of the gripper. The self-sensing gripper grasping objects with different weights. e) The corresponding resistance changes under different weights. f) Demonstration of shape-sensing ability of the gripper. The self-sensing gripper grasping different positions of a gourd-shape object. g) The corresponding resistance changes at different positions of the object. Photo credit: Bojian Zhang and Xudong Yang, Nanyang Technological University.

© 2022 The Authors. Advanced Intelligent Systems published by Wiley-VCH GmbH

with loads ranging from 0 to 200 g, and Figure 4b shows the different stages of resistance change within this load range. As shown, the resistance remains constant without loading and drops by ≈0.4% when the 50 g load is applied. When the load is removed, the structure recovers to its initial shape, and the resistance recovers to the original level. With increasing loads (100 and 200 g), the resistance drops to lower levels (by 1% and 2.5%, respectively) due to the larger deformation of our structure which results in lower resistance. The cyclic test shows good stability and sensitivity of our robotic structure as smart architectures. Unlike traditional structural sensing technologies that require extra sensors, our robotic structure achieves load sensing by the intrinsic contact resistance between particles, which saves manufacturing costs and enables fast deployment and large-area monitoring.

In addition to smart architectures, we explore the multifunctionality of our robotic structures in the application as fast-responsive and self-sensing soft grippers. Herein, we develop soft four-finger grippers from the robotic structure. Each finger shares an identical geometric design, while the particles in one of the four fingers are made conductive for self-sensing. With the fast shape-changing ability and variable stiffness, our gripper can adapt to and lift objects with arbitrary shapes and diverse weights ranging from less than 1 g to above 200 g (Figure 4b). With the self-sensing ability, our gripper can sense its holding weight without the need for extra sensors (Figure 4d,e). To obtain the sensing range of our gripper, we performed the sensitivity test with different weights (Figure S12, Supporting Information). As shown in Figure S12, Supporting Information, the resistance drops with the increase in weight (below 135 g). When the weight keeps increasing (above 135 g), the resistance remains stable and does not decrease. This is because the contact resistances between the conductive particles have saturated with increasing load. Besides detecting the weight of the object, we also demonstrate the potential of the gripper in identifying the shape of the object without visual feedback (Figure 4f,g). To keep the weight the same, we chose a gourd-shaped object with a fixed weight (50 g) and various radii at different heights. When we first place the object entirely enclosed by the gripper, the resistance drops by 20%. We then move the gourd all the way down to the top end of the object, and the reference resistance data are recorded to represent the different diameters of the object (Figure 4g). The resistance drops by ≈51%, ≈17%, and ≈32%, respectively, when it detects the largest diameter (54 mm), the neck region (30 mm), and the medium diameter (40 mm). This resistance change during grasping demonstrates the potential application for the unknown objects' shape recognition.

3. Conclusion

In this work, we develop robotic structures that can change shape, vary stiffness, and self-sense based on architectured particle assemblies. In contrast to traditional soft robots that achieve shape changing via intrinsic material or structural softness, our robotic structures achieve programmable shape changing and stiffness variation by tuning the interparticle contacts. Besides shape changing and variable stiffness, our robotic structures achieve self-sensing by monitoring the contact resistance between neighboring conductive particles. Unlike traditional solutions by attaching sensors to the actuation layer which may lead to delamination, our robotic structures achieve self-sensing by integrating conductive architectured particles into one monolithic structure.

Recent progress in additive manufacturing enables flexible and scalable manufacturing of these robotic structures. Various 3D printing methods (such as SLA, fused deposition modeling, selective laser sintering, etc.) and materials can be utilized to fabricate the architectured particles, while a broad choice of conductive coatings can be used to achieve sensing capability. In principle, it is feasible to scale our robotic materials up to meter scale via large-scale manufacturing, targeting different applications ranging from soft robotic applications to smart architectures, as demonstrated in Figure 4.

Despite these advantages, our robotic structures still have several aspects that can be optimized. 1) The rubber envelope and the architectured particles are fabricated separately due to manufacturing limits, which could be created via a multimaterial printing platform in the future. 2) The conductive layer could be achieved and optimized with cheaper conductive material to save cost in future applications. 3) Closed-loop control algorithms and wireless communication systems could enable the efficient and convenient operation of the sensing signals from our robotic structures, offering on-demand stiffening and structural sensing for broader applications, including in healthcare devices and haptic interfaces.

Finally, we believe our robotic structures with shape-changing, stiffness variation, and self-sensing functionality within a monolithic structure may provide more opportunities for smart materials and structures in next-generation robotic, medical, and architecture systems.

4. Experimental Section

Design and Fabrication of Robotic Structures: We first considered two trapezoidal particles with different tilting angles in contact. A central angle θ will be formed due to the difference between the two tilting angles (Equation (1))

If we fill the curved surface of a radius R with the upper surface of the particles, and the central angle θ is small enough, then the upper surface of the two particles could be considered colinear. Thus

$$D_1 + D_2 = 2R\theta \tag{4}$$

When the height of the particle is given, then the parameters of the trapezoidal particles are defined. With n pairs of the two particles assembled, a 1D curved surface with the central angle $(2n-1)\theta$ was displayed. We used SLA 3D printing (Form3, Formlab, USA) to create the architectured particles. This technique provides a high spatial resolution (25 μm) and yields parts with high geometrical fidelity, which is critical to making particles with consistent surface roughness. The 3D-printed structured particles were attached to a silicone–rubber film (Zhongyu Company, China) using silicone glue (Xinzhanxiang Adhesive Company, China). The thickness of the film was 0.2 mm. The initial distance between adjacent particles was 0.3 mm. Then a rubber bag was made to provide an air-tight space. A tube was then inserted into the bag to pop the air out. The tube was fixed to the bag to avoid its free and vibration movement in the bag. A pump (VP-30 L, JOANLAB, China) was connected to the tube for popping out air. The detailed dimensions and weights of robotic structures are listed (**Table 1**).

© 2022 The Authors. Advanced Intelligent Systems published by Wiley-VCH GmbH

Table 1. Dimensions and weights of robotic structures.

Sample	Dimensions [mm]	Weight [g] (With membrane)
Three-point bending samples	$h = 7.5$; $l = 10$	≈14.56
Dome surface	$h = 6$; lengths vary	≈49.35
Saddle surface	$h = 6$; lengths vary	≈38.51
Robotic arc shape surface	$h = 7.5$; $l = 30$	≈34.65
Robotic gripper	$h = 7.5$; $l = 10$	≈154.66 (With connector)

Table 2. Parameters used in the finite-element simulation.

Parameters	Density [g cm^{-3}]	Modulus [MPa]	Poisson's ratio	Friction coefficient between the indenter and the rubber	Friction coefficient between the particle and the rubber	Friction coefficient between the particles
Particle	1.2	2200	0.3	0.84	0.15	0.68
Membrane	1	13.6	0.48			

Design and Fabrication of Robotic Structures: We used sputter coating to fabricate the conductive particles using a commercial sputter coater (Polaron SC7620, Quorum Technologies, UK). The sputter-coating rate was 0.092 nm s^{-1}. A thin layer of gold was sputtered on the surface of the structured particles. To find the appropriate sputter-coating time, we performed four-point probe tests to evaluate the resistivity of the particle as the function of coating time (Figure S7, Supporting Information). The resistance reached a stable state when the coating time was 240 s. The obtained coating layer had a thickness of ≈22 nm.

Characterization and Measurements: We used a universal testing machine (MARK-10 with 25 N load cell, USA) to conduct quasistatic three-point bending tests. The diameters of the loading rod and the two supporting rods were all 10 mm. The span between the two supporting rods was 80 mm. The loading rate was 2 mm min^{-1}, the total loading displacement was 8 mm. To make the results consistent, the heights of the particle for the three tilting angles were 7.5 mm. The lengths of the medial sections were all set to 10 mm. For the piezoresistive characterization of the sample, the resistance data were collected by a two-probe method using a high-resolution digital multimeter (34465 A, Keysight Technologies, USA). The specimens used for three-point bending experiments and resistance measurement consisted of 12 particles, with an overall length of 12 cm along the medial section direction. In the three-point bending experiments, particles with three tilting angles (60°, 70°, and 80°) were adopted to explore the influence of the geometrical parameters. To estimate the mechanical contribution of the rubber envelope to the overall bending modulus, we considered the three-point pointing sample as a three-layer composite beam (membrane–particles–membrane). The upper limit of contribution from the rubber membranes on apparent bending stiffness can be calculated by the parameter $\alpha = \frac{E_m h_m^3 - E_m (h-2h_m)^3}{E^* h^3}$. Here, E_m is the effective elastic modulus of the rubber membrane, h_m is the membrane's thickness, h is the particle thickness, and E^* is the apparent bending modulus of our robotic structure obtained from experimental data. As h_m is much smaller than h, thus, we obtain that $\alpha \approx \frac{6E_m h_m}{E^* h}$. At zero negative pressure, E^*=2.14 MPa, and we obtained $\alpha \approx 1$. This means that the membrane dominates the modulus when the particles are not in contact. However, at the pressure of 80 kPa, E^*=31 MPa, we obtained $\alpha = 7\%$, which means that the membranes' contribution is much smaller than the contribution from particle contacts in our robotic structures at large negative pressures.

In the piezoresistive characterizations, samples with 3, 5, and 7 conductive particles were used to investigate the influence of numbers of particles on the sensing performance. The morphology of the surface was characterized by an optical microscope (Zeiss Axioskop microscope, Carl Zeiss, Germany) (Figure S6, Supporting Information) and laser scanning confocal microscope (VK-X1000, KEYENCE, Japan) (Figure S7, Supporting Information). It can be clearly seen that the surface of the structured particles had a layered structure, which is because of the layer-to-layer printing technique of SLA.

Finite-Element Simulation: The finite-element simulation was conducted using the commercial package ABAQUS 6.14/Explicit (Dassault Systèmes Simulia Corp., USA). In all the simulations in this report, the structured particles were meshed with a eight-node linear brick, reduced integration, hourglass control, and C3D8R element. To avoid the nonconvergence of the simulation, the membrane was meshed with Hex element shape using the sweep technique and the medial axis algorithms to minimize the mesh transition. The thickness of the membrane was set to be 0.2 mm, which is consistent with the experiment. For the properties of the rubber envelope, according to the data provided by the manufacturer (Zhongyu Company, China), the shore hardness of the rubber film was 65 A. However, in our fabrication process, we used silicone glue to fix the architectured particles on the rubber film, which was then connected by a soft tube to the vacuum source. Considering the influence of the glue layer on the rubber film and the soft tube, we used our three-point bending experimental data to fit the effective modulus of the rubber film with the glue layer in our finite-element simulation. The effective elastic modulus of the rubber layer with glue was 13.6 MPa. Detailed parameters used in the simulation are listed, and material properties of the 3D printed particles are obtained from the resin manufacturer (Formlabs Clear resin) (**Table 2**).

Supporting Information

Supporting Information is available from the Wiley Online Library or from the author.

Acknowledgements

This work was supported by MTC IRG award (M21K2c0118) and AME YIRG award (A2084c0162), both funded by Singapore Agency for Science, Technology and Research (A*STAR). Y. W. acknowledges the funding support from Nanyang Technological University NAP award (020482).

Conflict of Interest

The authors declare no conflict of interest.

© 2022 The Authors. Advanced Intelligent Systems published by Wiley-VCH GmbH

Author Contributions

X.Y. and Y.W. developed the overall concept, designed the experiments, and analyzed the data. Y.W. supervised the project. X.Y. fabricated and characterized the samples. Z.W. conducted the numerical analysis on the contacts between particles. B.Z. and X.Y took photos and videos. X.Y. and T. C. conducted the finite-element simulation. H.L. conducted the sputter-coating fabrication. K.W. conducted the optical microscope and laser microscope characterization. X.Y., G.W., and H.W. designed the grippers. X.Y., Y.W., and Z.W. wrote the manuscript and the supplementary documents. All the authors contributed to the discussion, data analysis, and edit of the manuscript.

Data Availability Statement

The data that support the findings of this study are available from the corresponding author upon reasonable request.

Keywords

architectured materials, robotic structures, self-sensing, stiffness tunable, 3D printing

Received: August 2, 2022
Revised: September 13, 2022
Published online: October 9, 2022

[1] M. A. McEvoy, N. Correll, *Science* **2015**, *347*, 1261689.
[2] a) J. H. G. Jessica, A.-C. Liu, *Sci. Adv.* **2019**, *5*, eaaw2897; b) D. Hwang, E. J. Barron III, A. T. Haque, M. D. Bartlett, *Sci. Robot.* **2022**, *7*, eabg2171; c) A. Kotikian, C. McMahan, E. C. Davidson, J. M. Muhammad, R. D. Weeks, C. Daraio, J. A. Lewis, *Sci. Robot.* **2019**, *4,* eaax7044.
[3] a) W. Pang, X. Cheng, H. Zhao, X. Guo, Z. Ji, G. Li, Y. Liang, Z. Xue, H. Song, F. Zhang, Z. Xu, L. Sang, W. Huang, T. Li, Y. Zhang, *Nat. Sci. Rev.* **2020**, *7*, 342; b) X. Ning, X. Yu, H. Wang, R. Sun, R. Corman, H. Li, C. M. Lee, Y. Xue, A. Chempakasseril, Y. Yao, *Sci. Adv.* **2018**, *4*, eaat8313.
[4] a) B. Gorissen, D. Melancon, N. Vasios, M. Torbati, K. Bertoldi, *Sci. Robot.* **2020**, *5*, eabb1967; b) A. Rafsanjani, Y. Zhang, B. Liu, S. M. Rubinstein, K. Bertoldi, *Sci. Robot.* **2018**, *3*, eaar7555.
[5] a) Y. Zhao, C.-Y. Lo, L. Ruan, C.-H. Pi, C. Kim, Y. Alsaid, I. Frenkel, R. Rico, T.-C. Tsao, X. He, *Sci. Robot.* **2021**, *6*, eabd5483; b) H. Liu, H. Tian, X. Li, X. Chen, K. Zhang, H. Shi, C. Wang, J. Shao, *Sci. Adv.* **2022**, *8*, eabn5722; c) A. Heiden, D. Preninger, L. Lehner, M. Baumgartner, M. Drack, E. Woritzka, D. Schiller, R. Gerstmayr, F. Hartmann, M. Kaltenbrunner, *Sci. Robot.* **2022**, *7*, eabk2119; d) H. Wang, M. Totaro, L. Beccai, *Adv. Sci.* **2018**, *5*, 1800541.
[6] T. van Manen, S. Janbaz, A. A. Zadpoor, *Mater. Today* **2018**, *21*, 144.
[7] X. P. Hao, Z. Xu, C. Y. Li, W. Hong, Q. Zheng, Z. L. Wu, *Adv. Mater.* **2020**, *32*, 2000781.
[8] Y. Kim, J. van den Berg, A. J. Crosby, *Nat. Mater.* **2021**, *20*, 1695.
[9] a) D. P. Holmes, *Curr. Opin. Colloid Interface Sci.* **2019**, *40*, 118; b) M. Liu, L. Domino, D. Vella, *Soft Matter* **2020**, *16*, 7739.
[10] F. Hannard, M. Mirkhalaf, A. Ameri, F. Barthelat, *Sci. Robot.* **2021**, *6*, eabf9710.
[11] J. Yan, Z. Xu, P. Shi, J. Zhao, *Soft Robot* **2021**2022, *9*, 399.
[12] a) A. Lendlein, *Sci. Robot.* **2018**, *3*, eaat9090; b) Q. Zhao, W. Zou, Y. Luo, T. Xie, *Sci. Adv.* **2016**, *2*, 1501297.
[13] M. Manti, V. Cacucciolo, M. Cianchetti, *IEEE Robot. Autom. Mag.* **2016**, *23*, 93.
[14] S. Shian, K. Bertoldi, D. R. Clarke, *Adv. Mater.* **2015**, *27*, 6814.
[15] Y. F. Zhang, N. Zhang, H. Hingorani, N. Ding, D. Wang, C. Yuan, B. Zhang, G. Gu, Q. Ge, *Adv. Funct. Mater.* **2019**, *29*, 1970098.
[16] J. A. Jackson, M. C. Messner, N. A. Dudukovic, W. L. Smith, L. Bekker, B. Moran, A. M. Golobic, A. J. Pascall, E. B. Duoss, K. J. Loh, *Sci. Adv.* **2018**, *4*, eaau6419.
[17] J. Biggs, K. Danielmeier, J. Hitzbleck, J. Krause, T. Kridl, S. Nowak, E. Orselli, X. Quan, D. Schapeler, W. Sutherland, J. Wagner, *Angew. Chem., Int. Ed. Engl.* **2013**, *52*, 9409.
[18] a) Y. Wang, L. Li, D. Hofmann, J. E. Andrade, C. Daraio, *Nature* **2021**, *596*, 238; b) E. Brown, N. Rodenberg, J. Amend, A. Mozeika, E. Steltz, M. R. Zakin, H. Lipson, H. M. Jaeger, *Proc. Natl. Acad. Sci.* **2010**, *107*, 18809; c) D. S. Shah, E. J. Yang, M. C. Yuen, E. C. Huang, R. Kramer-Bottiglio, *Adv. Funct. Mater.* **2021**, *31*, 2006915; d) M. Brancadoro, M. Manti, S. Tognarelli, M. Cianchetti, *Soft Robot.* **2020**, *7*, 663.
[19] a) Y. Li, Y. Chen, Y. Yang, Y. Wei, *IEEE Trans. Robot.* **2017**, *33*, 446; b) D. C. F. Li, Z. Wang, J. Zhou, Y. H. Liu, *Soft Robot* **2021**, *8*, 720; c) P. Aejmelaeus-Lindström, J. Willmann, S. Tibbits, F. Gramazio, M. Kohler, *Granular Matter* **2016**, *18*.
[20] a) M. Li, A. Pal, A. Aghakhani, A. Pena-Francesch, M. Sitti, *Nat. Rev. Mater.* **2022**, *7*, 235; b) W. Dou, G. Zhong, J. Cao, Z. Shi, B. Peng, L. Jiang, *Adv. Mater. Technol.* **2021**, *6*, 2100018.
[21] M. Amjadi, M. Sitti, *Adv. Sci.* **2018**, *5*, 1800239.
[22] A. Pal, V. Restrepo, D. Goswami, R. V. Martinez, *Adv. Mater.* **2021**, *33*, 2006939.
[23] H. R. Lim, H. S. Kim, R. Qazi, Y. T. Kwon, J. W. Jeong, W. H. Yeo, *Adv. Mater.* **2020**, *32*, 1901924.
[24] a) F. Barthelat, *Int. Mater. Rev.* **2016**, *60*, 413; b) M. Mirkhalaf, T. Zhou, F. Barthelat, *Proc. Natl. Acad. Sci. U S A* **2018**, *115*, 9128; c) C. Gao, J. Kiendl, *Mater. Des. Process. Commun.* **2019**, *1*, 31; d) M. Mirkhalaf, A. Sunesara, B. Ashrafi, F. Barthelat, *Int. J. Solids Struct.* **2019**, *158*, 52.
[25] A. Bahmani, J. W. Pro, F. Hannard, F. Barthelat, *Matter* **2022**, *5*, 899.
[26] T. Siegmund, F. Barthelat, R. Cipra, E. Habtour, J. Riddick, *Appl. Mech. Rev.* **2016**, *68*, 040803.
[27] F. Pan, Y. Li, Z. Li, J. Yang, B. Liu, Y. Chen, *Adv. Mater.* **2019**, *31*, 1900548.
[28] M. Weizmann, O. Amir, Y. J. Grobman, *Autom. Construct.* **2016**, *72*, 18.
[29] A. V. Dyskin, Y. Estrin, A. J. Kanel-Belov, E. Pasternak, *Philos. Mag. Lett.* **2003**, *83*, 197.
[30] Z. Wang, P. Song, F. Isvoranu, M. Pauly, *ACM Trans. Graph.* **2019**, *38*, 1.
[31] B. Aktaş, Y. S. Narang, N. Vasios, K. Bertoldi, R. D. Howe, *Adv. Funct. Mater.* **2021**, *31*, 2007554.
[32] J. T. Auletta, G. J. LeDonne, K. C. Gronborg, C. D. Ladd, H. Liu, W. W. Clark, T. Y. Meyer, *Macromolecules* **2015**, *48*, 1736.
[33] a) T. Chen, M. Pauly, P. M. Reis, *Nature* **2021**, *589*, 386; b) W. Shan, T. Lu, C. Majidi, *Smart Mater. Struct.* **2013**, *22*, 085005; c) T. Li, J. Wang, L. Zhang, J. Yang, M. Yang, D. Zhu, X. Zhou, S. Handschuh-Wang, Y. Liu, X. Zhou, *J. Mater. Chem. B* **2017**, *5*, 5726.
[34] J. Choi, S. Han, M. Baliwag, B. H. Kim, H. Jang, J.-T. Kim, I. Hong, T. Kim, S. M. Kang, K.-T. Lee, D. Kang, J. A. Rogers, *Extreme Mech. Lett.* **2022**, *50*, 101537.
[35] L. Romano-Brandt, E. Salvati, E. Le Bourhis, T. Moxham, I. P. Dolbnya, A. M. Korsunsky, *Surf. Coat. Technol.* **2020**, *381*, 125142.
[36] a) T. Li, Z. Suo, *Int. J. Solids Struct.* **2007**, *44*, 1696; b) S. H. Oh, M. Legros, D. Kiener, P. Gruber, G. Dehm, *Acta Mater.* **2007**, *55*, 5558.
[37] a) M. C. Lin, H. H. Huang, *J. Prosthodont.* **2014**, *23*, 540; b) M. Nordström, A. Johansson, E. S. Nogueron, B. Clausen, M. Calleja, A. Boisen, *Microelectron. Eng.* **2005**, *78*, 152; c) W. Li,

© 2022 The Authors. Advanced Intelligent Systems published by Wiley-VCH GmbH

R. Charters, B. Luther-Davies, L. Mar, *Appl. Surf. Sci.* **2004**, *233*, 227; d) N. Lu, Z. Suo, J. J. Vlassak, *Acta Mater.* **2010**, *58*, 1679.
[38] I. Polonsky, L. Keer, *Wear* **1999**, *231*, 206.
[39] J. G. Simmons, *J. Appl. Phys.* **1963**, *34*, 1793.
[40] J. Kim, R. Kumar, A. J. Bandodkar, J. Wang, *Adv. Electron. Mater.* **2017**, *3*, 1600260.
[41] a) H. S. Tzou, H. J. Lee, S. M. Arnold, *Mech. Adv. Mater. Struct.* **2004**, *11*, 367; b) M. Sobczyk, S. Wiesenhütter, J. R. Noennig, T. Wallmersperger, *J. Intell. Mater. Syst. Struct.* **2021**, *33*, 379.
[42] E. Demircilioglu, E. Teomete, O. E. Ozbulut, *J. Intell. Mater. Syst. Struct.* **2019**, *31*, 127.

© 2022 The Authors. Advanced Intelligent Systems published by Wiley-VCH GmbH